# Is heteroatom doping of activated carbons always a good strategy for enhancing CO2 adsorption?

R. Morales-Ospino, R.L.S. Canevesi, S. Schaefer, A. Celzard, V. Fierro

# Is heteroatom doping of activated carbons always a good strategy for enhancing $CO_2$ adsorption?

R. Morales-Ospino[1,⊥], R. L. S. Canevesi[1*,⊥], S. Schaefer[1], A. Celzard[1,2], V. Fierro[1,*]

[1] Université de Lorraine, Centre National de la Recherche Scientifique (CNRS), Institut Jean Lamour (IJL), F-88000, Épinal, France.

[2] Institut Universitaire de France (IUF), 75231 Paris, France

*Corresponding authors: rafael_canevesi@hotmail.com, vanessa.fierro@univ-lorraine.fr

[⊥]These two authors contributed equally to this work

**Abstract**

This study shows the substantial impact of textural properties, with greater weight than N-doping, on $CO_2$ adsorption by carbon materials over a pressure range from 1 to 25 bar and a temperature range from 273 to 323 K. It also highlights the importance of providing volumetric $CO_2$ adsorption capacities when presenting newly developed materials. These results were obtained by exploring the influence of O- and N-doping on $CO_2$ uptake on 14 activated carbons (ACs) with distinct specific surface areas, from 1736 to 3200 $m^2$ $g^{-1}$, and micropore fractions from 37 to 96%. Based on 3 commercial ACs, N content was maximized by hydrogen peroxide oxidation and urea treatment, reaching around 11 at.%. O-N-doping mainly impacted the largest pores, reducing material textural properties and thus $CO_2$ adsorption, although it improved $CO_2/N_2$ selectivity, especially up to 5 bar and between 273 and 323 K. The contribution of heteroatoms to $CO_2$ uptake was particularly significant at low pressures and high temperatures, with threshold pressures increasing at higher temperatures. Breakthrough simulations were also carried out and the results demonstrate that, despite a lower specific surface area, the O-doped material exhibited longer breakthrough times than its commercial counterpart. This can be attributed to a balance between $CO_2$ adsorption capacity, governed by the textural properties, and tap density, i.e., adsorption capacity per unit volume.

*Keywords*: *$CO_2$ capture, adsorption, nitrogen-doping, oxygen-doping, activated carbons.*

## 1. Introduction

The concentration of $CO_2$ in the atmosphere has been increasing rapidly since the industrial revolution, and is predicted to reach 570 ppm by 2100, according to numerous studies[1,2]. $CO_2$ is a major contributor to the current climate change observed worldwide[3,4]. As a result, the scientific community and governments worldwide are making significant efforts to find solutions[5]. Two main approaches have been adopted, namely, $CO_2$ emission reduction and $CO_2$ capture and storage (CCS)[6–9]. CCS is considered a key method to reduce $CO_2$ emissions in the industrial sector[10]. Studies suggest that these technologies have the potential to eliminate around 20% of $CO_2$ emissions by 2050[10].

Various carbon capture technologies, including adsorption, absorption and membranes, are being applied to the CCS processes[11,12]. Adsorption, in particular, is receiving increasing attention due to its relatively low energy consumption and lack of toxic by-products production. This makes it a more environmentally-friendly option compared to traditional absorption-based capture systems[13]. A variety of high-surface-area materials have been used as adsorbents for $CO_2$ capture, including zeolites[14,15], metal-organic frameworks (MOFs)[15,16], porous polymers[17] and carbon materials[18,19].

Carbon materials are used as adsorbents in CCS due to their low cost, high chemical and mechanical stability, and ease of manufacture. They can be derived from petrochemical sources such as coal[20–23] or produced by the pyrolysis of various C-containing materials, including bio-sourced precursors[24–26], with or without subsequent chemical or physical activation[20]. Carbon materials comprising alkaline functional groups, such as nitrogen and oxygen species, have emerged as promising candidates for CCS technologies due to their enhanced $CO_2$ adsorption capacities[27–30]. Moreover, high-surface-area activated carbons (ACs), having a considerable amount of ultramicropores (pores width $w < 0.7$ nm) and supermicropores ($0.7 < w < 2$ nm), are of particular interest. Indeed, the micropore volume is closely related to surface area and so therefore to $CO_2$ adsorption capacity[31–35].

Most studies into the development of materials for $CO_2$ adsorption are conducted using manometric devices designed for textural characterization[36–42]. These studies typically present adsorption data at 0 °C (or at best room temperature), using an ice bath to maintain this temperature, and report isotherms up to 1 atm. Given that CCS processes typically operate at temperatures above ambient levels[43,44], it is

important to understand the thermal effects on $CO_2$ adsorption when using chemically modified adsorbents featuring nitrogen- (N) and/or oxygen- (O) doping. Although the chemical and textural properties of adsorbents are known to have an impact on $CO_2$ adsorption capacity, their implications for practical processing conditions remain relatively unexplored. Furthermore, the specific conditions under which heteroatom-doping can enhance $CO_2$ uptake are still unclear. The main objective of this study is therefore to examine the impact of the presence of heteroatoms, in particular N and O at varying percentages, on $CO_2$ adsorption under different temperature and pressure conditions. The study aims to understand how the inclusion of these heteroatoms affects $CO_2$ adsorption capacity to explore optimal conditions for enhanced $CO_2$ capture.

Another relevant aspect investigated in this study is the significance of volumetric capacities in the context of gas adsorption, as they play a crucial role in determining the volume of the adsorption column. Indeed, the tap density of the materials was systematically determined herein, and the material chosen for breakthrough experiments was carefully selected with this crucial factor in mind, a point that is often overlooked in favor of gravimetric capacities.

In this paper, three commercial ACs were used as precursors for N- and/or O-doped ACs, which were prepared via chemical treatment with urea, with or without a preliminary oxidation step to increase O content and reactivity. The textural properties and elemental compositions of the resulting materials were characterized, and their $CO_2$ and $N_2$ adsorption isotherms were measured at temperatures of 273, 298, and 313 K up to 25 bar in order to consider a dry post-combustion carbon capture scenario. The selectivity of $CO_2$ capture over $N_2$ was also evaluated to reveal the conditions under which heteroatom doping can provide a better separation factor. Adsorption data were used to model breakthrough curves under different temperature and pressure conditions. An analysis was performed to understand the effect of N-doping on adsorption properties as a function of temperature and pressure.

## 2. Materials and methods

### 2.1. Activated carbons

The precursors for the O- and/or N-doped adsorbents were three commercially available ACs, namely MSP20X, MSC30, and CW30. The first two ACs were obtained from Kansai Coke & Chemicals™ (Japan), while the third was supplied by Silcarbon & Aktivkohle (Germany). According to the information furnished by the suppliers, the three ACs have well-developed textural properties, with BET areas, $A_{BET}$, much higher than 1500 $m^2\ g^{-1}$.

### 2.2. Chemical modifications

Oxygen- and/or nitrogen-doped activated carbons were prepared from the three aforementioned commercial materials by chemical and/or thermal treatment using three different routes, as illustrated in Figure 1.

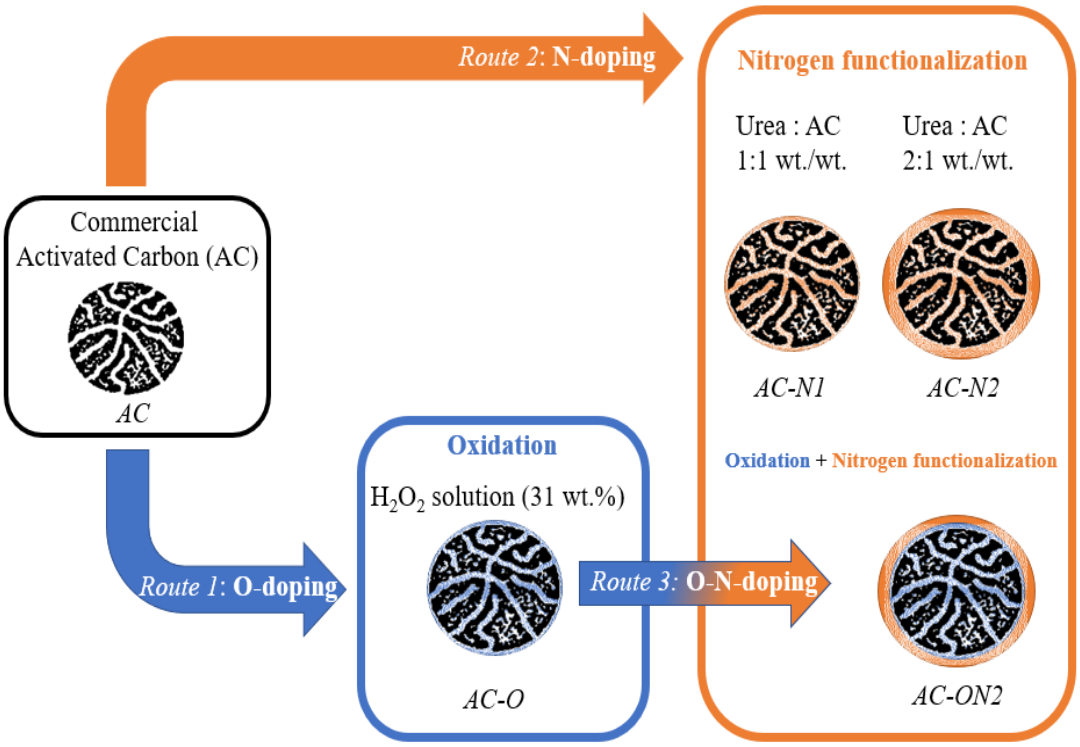


Figure 1. Chemical modification routes of pristine carbon materials.

*Route 1*: **O-doped carbons** were obtained by oxidizing 3g of AC with a solution of hydrogen peroxide (31 wt.%) at room temperature. To this end, the pristine materials were treated with 10 mL of $H_2O_2$

solution, adding it at one-hour intervals until a total of 30 mL was added with some stirring. ACs obtained from this oxidation route were labeled *AC-O* (e.g., for MSP20X→MSP20X-O)

*Route 2*: **N-doped carbons** were prepared by mixing 1g of AC with urea powder (99.5 %, ACROS), then subjecting the blend to heat treatment in a tubular furnace. Beforehand, the urea crystals were ground using a PM 100 planetary ball mill (RETSCH) and then sieved to obtain particle sizes below 100 µm. The urea / carbon weight ratio was either 1 or 2, and the mixture was subjected to heat treatment in an oven up to 623 K at a rate of 5 K $min^{-1}$. This heat treatment was carried out under a synthetic air atmosphere with a flow rate of 50 $cm^3$ $min^{-1}$. The final temperature was maintained for 3 h, after which the samples were cooled to room temperature under the same air flow. Finally, the materials were washed with hot water until neutral pH and dried for 24 h in a ventilated oven at 378 K. N-doped carbons following *route 2* were labeled *AC-N1* or *AC-N2* with the numbers 1 and 2 indicating the urea / carbon ratio (e.g., for MSP20X→MSP20X-N1 or MSP20X-N2).

*Route 3:* **O-N-doped carbons** were obtained by mixing 1g of O-doped carbons from *route 1* with 2g of urea powder, following the same synthesis protocol used in *route 2*. The resulting materials were labeled *AC-ON2* (e.g., for MSP20X→MSP20X-ON2).

### 2.3. Adsorbent Characterization

$N_2$ and $H_2$ adsorption isotherms at 77 K were acquired using an ASAP 2020 automatic adsorption device (MICROMERITICS). $H_2$ at 77 K was selected as probe molecule for characterizing the adsorbent materials due to its rapid diffusion into ultramicropores, enabling the acquisition of a more comprehensive pore size distribution (PSD). The reason lies in the supercritical state of $H_2$ under such conditions and its smaller molecular size than $N_2$. Furthermore, $H_2$ exhibits reduced susceptibility to interactions with polar surface sites due to its smaller quadrupole moment, which distinguishes it from other probe molecules like $CO_2$ at 273 K, which can also penetrate in ultramicropores[45].

The specific surface area was calculated from $N_2$ isotherms using the BET equation ($A_{BET}$, $m^2$ $g^{-1}$), or from both $N_2$ and $H_2$ isotherms using the two-dimensional non-local density functional theory (2D-NLDFT) to determine the specific surface area, $S_{NLDFT}$ ($m^2$ $g^{-1}$). The total pore volume ($V_T$, $cm^3$ $g^{-1}$),

micropore volume ($V_{\mu\text{-}NLDFT}$, $cm^3\ g^{-1}$), pore size distribution (PSD), and average micropore size ($L_0$, nm) were also calculated using the same 2D-NLDFT model. The mesopore volume ($V_{MES}$, $cm^3\ g^{-1}$) was estimated by subtracting $V_{\mu\text{-}NLDFT}$ from $V_T$.

Surface chemistry analyses were conducted by X-ray photoelectron spectroscopy (XPS) using an ESCAPlus OMICROM system equipped with a hemispherical electron energy analyzer with an analysis area measuring 1.75 mm × 2.75 mm. The spectrometer was operated at 10 kV and 15 mA and used a non-monochromatized Mg X-ray source (1253.6 eV) under vacuum ($< 7 \times 10^{-9}$ mbar). Data processing software (CASA) was employed for smoothing, Shirley-type background subtraction, peak fitting and quantification. The carbon, hydrogen, nitrogen and oxygen contents (wt.%) of the samples were determined using a Vario EL cube analyzer (Elementar), in which ~2 mg of each sample are burned at 1700 °C in a mixed atmosphere of helium and oxygen. The gases generated are then selectively separated with a chromatographic column and measured using a thermal conductivity detector (with a sensitivity of approximately 40 ppm). This method enables the C, H, and N contents of the materials to be calculated. In a second experiment, the O content is obtained by reducing the oxygen-containing combustion gases to CO, and quantifying the latter.

Tap densities of the different carbonaceous materials were determined using an AUTOTAP device (QUANTACHROME). The analysis was performed as follows: a graduated glass cylinder with a diameter of 10 mm was filled with a known weight of sample. A tapping program with a frequency of 260 taps $min^{-1}$ was run for 20 min. The final volume was obtained from the graduated cylinder, and the tap density was calculated as the ratio between the weight and the final volume.

### 2.4. High-pressure adsorption isotherms

Adsorption isotherms of $CO_2$ and $N_2$ were carried out using the HPVA II high-pressure manometric device (MICROMERITICS) at temperatures of 273, 298 and 323 K, up to 25 bar. Prior to measurements, samples were degassed under vacuum at 383 K and $5 \times 10^{-6}$ mbar for 12 hours. A sample cell with a volume of 10 $cm^3$ was loaded with approximately 1g of carbon. After evacuation, the pressure was increased incrementally to the target pressure level, up to 25 bar. To improve accuracy, the contribution of the empty cell was systematically measured and subtracted from all data.

The single experimental equilibrium data were fitted to the Sips[46] adsorption model, as specified in the supplementary information SI1. The binary equilibria for $CO_2/N_2$ gas mixture were predicted by the Ideal Adsorbed Solution Theory (as detailed in SI1). The predicted multicomponent data allowed us to calculate the selectivity of the materials, preferential adsorption of $CO_2$ over $N_2$ as described in SI1.

The isosteric heat of adsorption, $Q_{st}$ (kJ $mol^{-1}$), was determined using the Clausius-Clapeyron equation (1) along with the Sips model fit.

$$-\frac{Q_{st}}{R} = \frac{\partial \ln(P)}{\partial\left(1/T\right)} \quad (1)$$

where $R$ is the universal gas constant (0.08314 L bar $mol^{-1}$ $K^{-1}$), $P$ is the absolute pressure (bar) and $T$ is the temperature (K).

### 2.5. Systematic study of the effect of the heteroatom content on $CO_2$ adsorption

To better understand how textural properties and surface chemistry contribute to $CO_2$ adsorption, a mathematical regression analysis was performed. Pore volumes $V$ ($cm^3$ $g^{-1}$) of the materials were split into 3 different categories according to the average pore size $L$ (nm), in line with the IUPAC classification: $V_{<0.7}$ (ultramicropores), $V_{0.7<w<0.2}$ (supermicropores) and $V_{2<w<50}$ (mesopores). A coefficient was then assigned to each range to represent its contribution to the adsorption process (*a*, *b* and *c*.). Additionally, the contribution of surface chemistry was determined by including the heteroatom content (N+O content by XPS, $C_{N+O}$) with a coefficient called *d*. This allowed the adsorption capacity $q_{co_2}^{MODEL}$ to be expressed mathematically as in Equation (2):

$$q_{co_2}^{MODEL} = a\, V_{w<0.7} + b\, V_{0.7<w<2} + c\, V_{2<w<50} + d\, C_{N+O} \quad (2)$$

To determine the coefficients (*a*, *b*, *c* and *d*) of Eq. (2) at different pressures and temperatures, multiple linear regression was performed on the experimental data. The coefficients were calculated for a total of eight different pressures, spanning from 0.25 to 25 bar, at three distinct temperatures (273, 298 and 323 K).

### 2.6. Modeling of breakthrough curves

The mathematical modeling used in this study to simulate single $CO_2$ breakthrough curves at different temperatures and pressures is based on validated models from previous works on adsorption[47–49]. The mathematical model considered the following assumptions:

- Ideal gas behavior
- Heat, mass and momentum transport are only considered in the axial direction
- The Ergun equation can be used to describe momentum balance
- A bi-Linear Driving Force (bi-LDF) model to describe diffusion in both the macropore and micropore region
- The void fraction, cross section and adsorbent properties are the same in all columns

The model incorporates mass, energy, and momentum balance equations, which are detailed in SI2. The system of partial differential equations was solved with gPROMS software from Siemens (UK) using a third-order orthogonal collocation method on a finite basis in the axial direction.

## 3. Results and discussion

### 3.1. Doping quantification

Heteroatom doping leads to a loss of material that significantly affects the oxidation process, resulting in an O-doped carbon yield of around 80%. Conversely, treatment with urea results in a significantly higher yield of N-doped carbon, exceeding 95%. X-ray photoelectron spectroscopy (XPS) was conducted on all materials, including the initial ACs, to quantify N and O contents and verify the effective doping of the modified materials. Figure 2a illustrates that the untreated ACs had a negligible presence of N on their surface (limit of quantification 1 at.%), while the three commercial ACs already contained O with atomic percentages (at. %) ranging from 2.8 to 6.1. Figure 2a confirms the successful N- and O-doping via *routes 1* and *2*, as evidenced by the noticeable increase in N and O contents. The nitrogen content in the N-doped ACs using a urea / carbon weight ratio of 1 ranged from 4% to 6%, whereas the N content varied from 6.1% to 11% in those with a ratio of 2. In contrast, when the amount of urea was doubled in *route 2*, a corresponding proportional increase in the surface N percentage was

not observed, as is evident in the *AC-N2* carbon materials. The ACs modified through *route 3* had N contents ranging from 8.3% to 11.4%. However, the addition of heteroatoms did not consistently result in an overall increase in the combined N+O content compared with the *AC-N2* materials. The exception is sample MSC30-ON2, for which the initial O content appears to influence subsequent nitrogen incorporation; this might be attributed to the Hofmann rearrangement mechanism, as previously demonstrated by several authors[50,51].

The results of elemental analysis (EA), presented in Figure 2b in atomic percent (at. %), validate the incorporation of both O and N into the bulk composition of the carbons. While the trends observed by XPS and EA analysis align, O and N contents were higher in the bulk, as determined by EA, compared to surface measurements by XPS. This discrepancy becomes more pronounced with increasing heteroatom content, as shown in SI3 d. The complete elemental analysis data (both in weight and atomic percentages) are presented in the Supporting Information SI3, including the C content in addition to those for N, O and H.

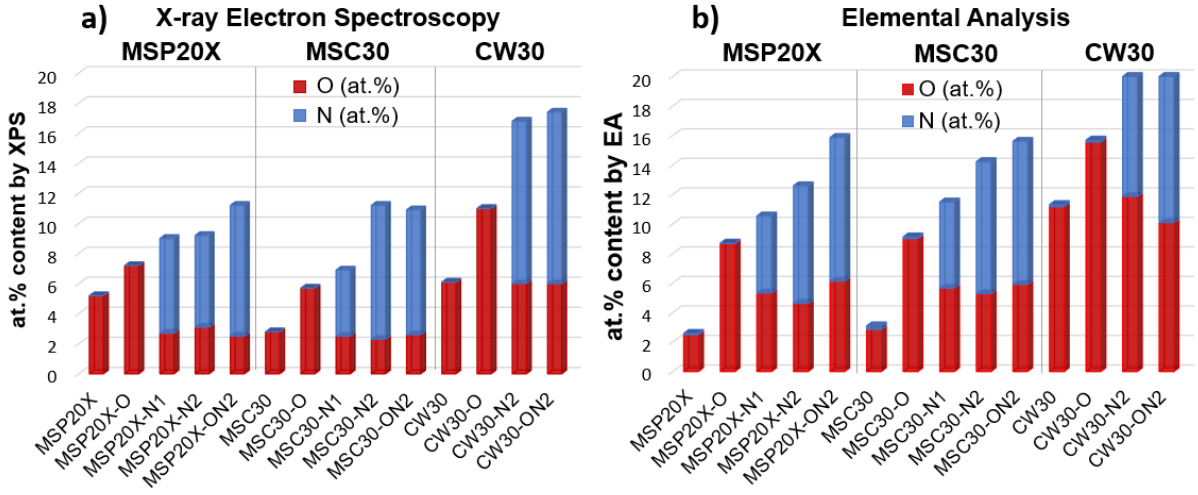


Figure 2. (a) Atomic contents (at. %) of O and N obtained by X-ray Photoelectron Spectroscopy (XPS) and b) elemental analysis in atomic content (at. %) for O, N and H.

The deconvolution of the XPS analysis of sample MSP20X-ON2 is presented as an example and revealed the presence of specific types of O and N functional groups, which are illustrated in Figures 3a and 3b, respectively.

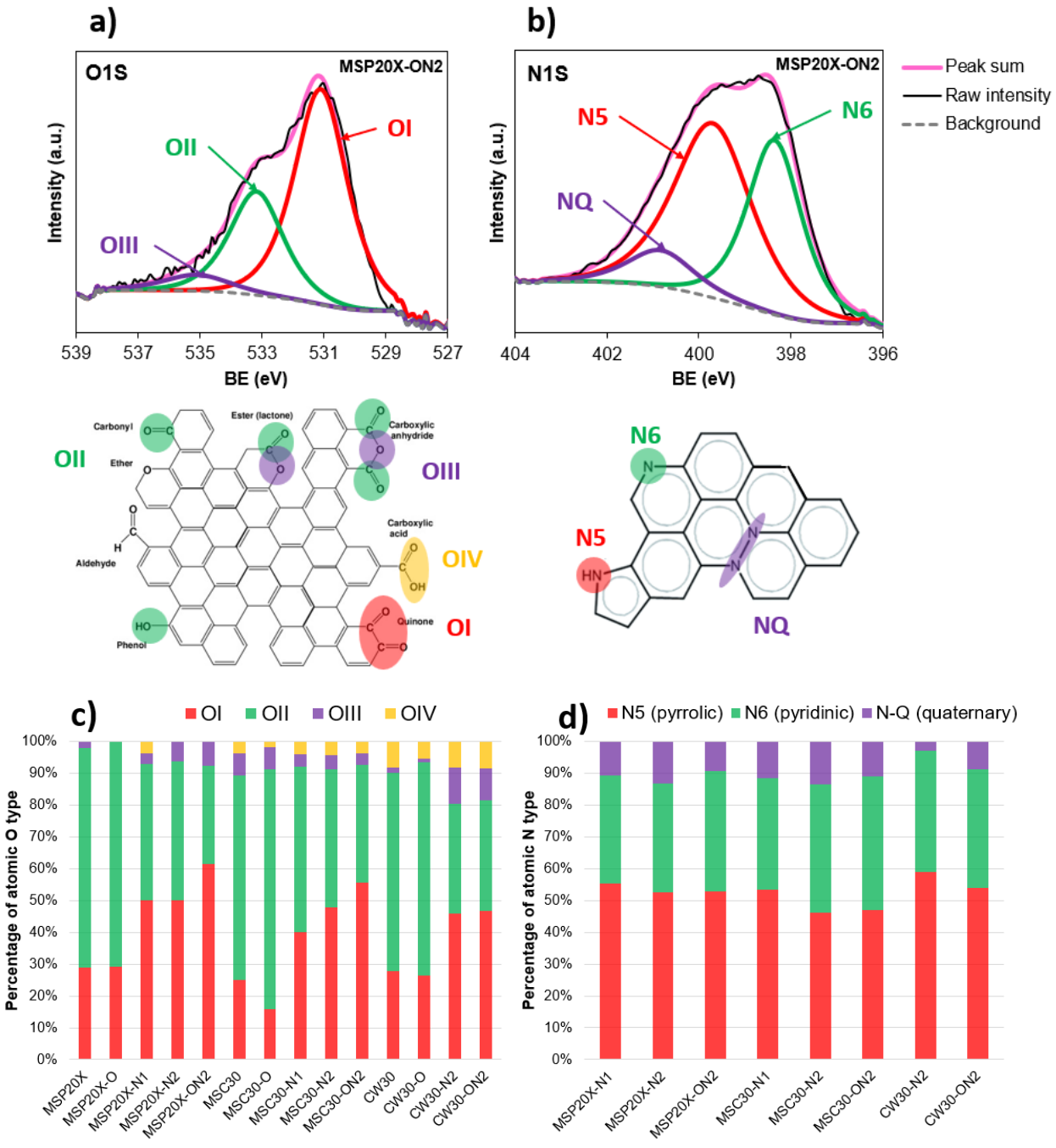


Figure 3. Example of deconvolution of the (a) O 1s and (b) N 1s regions of sample MSP20X-ON2. c) Atomic percentages of oxygen groups: OI (quinones), OII (carbonyl esters, acid anhydrides and hydroxyls), OIII (non-carbonyl esters and anhydrides) and OIV (carboxylic acids); d) atomic percentages of nitrogen groups: N5 (pyrrolic groups), N6 (pyridinic groups) and N-Q (quaternary groups).

Figure 3a shows typical O species, including OI (oxygen in quinones), OII (carbonyl oxygen in esters, acid anhydrides and hydroxyls), OIII (non-carbonyl oxygen in esters and anhydrides), and OIV (oxygen in carboxylic acids)[24]. The deconvolution of sample MSP20X-ON2 proved the presence of OI,

OII and OIII species, but no OIV was identified. Similarly, N functional groups were identified as shown in Figure 3b: pyrrolic (N5), pyridinic (N6), and quaternary (NQ) nitrogen groups[52,53].

The quantification in atomic percent (at. %) of O and N functional groups is shown in Figures 3c and 3d, respectively. OI and OII functional groups were found to be the most predominant, with OII type accounting for 62-69%, while N5 and N6 accounted for over 80% of the N content. OI and OII groups are common in the starting materials or precursor compounds used for the synthesis of activated carbons. These O species may already be present in the initial carbonaceous material or introduced during the carbonization or activation process The pre-oxidation treatment (*route 1*) resulted in a clear increase in O content, which is consistent with previous reports using $H_2O_2$ as an oxidizer[54,55]. It is noteworthy that the oxidation process primarily leads to an increase in the percentage of OII groups. The full XPS spectra in the O1s and N1s regions for the three commercial ACs and their modification is shown in SI3.

Although not plotted, the high-resolution C1s spectra were deconvoluted into five peaks, which were labeled from CI to CV. CI was assigned to $Csp^2$ in hydrocarbons, aromatics and aliphatics. CII was assigned to $Csp^3$ and C–O single bonds associated with ethers, phenols and anhydrides. CIII corresponded to C=O double bonds in carbonyls and quinones. The CIV and CV peaks were assigned to C–O single bonds in carboxylic groups and plasmon losses or shake-up π-π satellites, respectively[52,56,57]. The distribution of atomic carbon types, as well as the corresponding O- and N-functional groups, are presented in Table SI4 in the supplementary information.

### 3.2. Textural properties

SI5 shows $N_2$ and $H_2$ adsorption-desorption isotherms and corresponding pore size distributions for all samples. $N_2$ isotherms of pristine and doped MSP20X and MSC30 were characterized as Type I, indicating microporous materials according to the IUPAC classification[58]. Conversely, the isotherms for pristine and derived CW30 ACs were identified as type IV and displayed a hysteresis loop at $P/P_0$ above 0.50, suggesting the existence of capillary condensation in the mesopores.

Using $N_2$ and $H_2$ adsorption isotherms, the textural properties were determined by applying the 2D-NLDFT method, and the results are shown in Figures 4a and b.

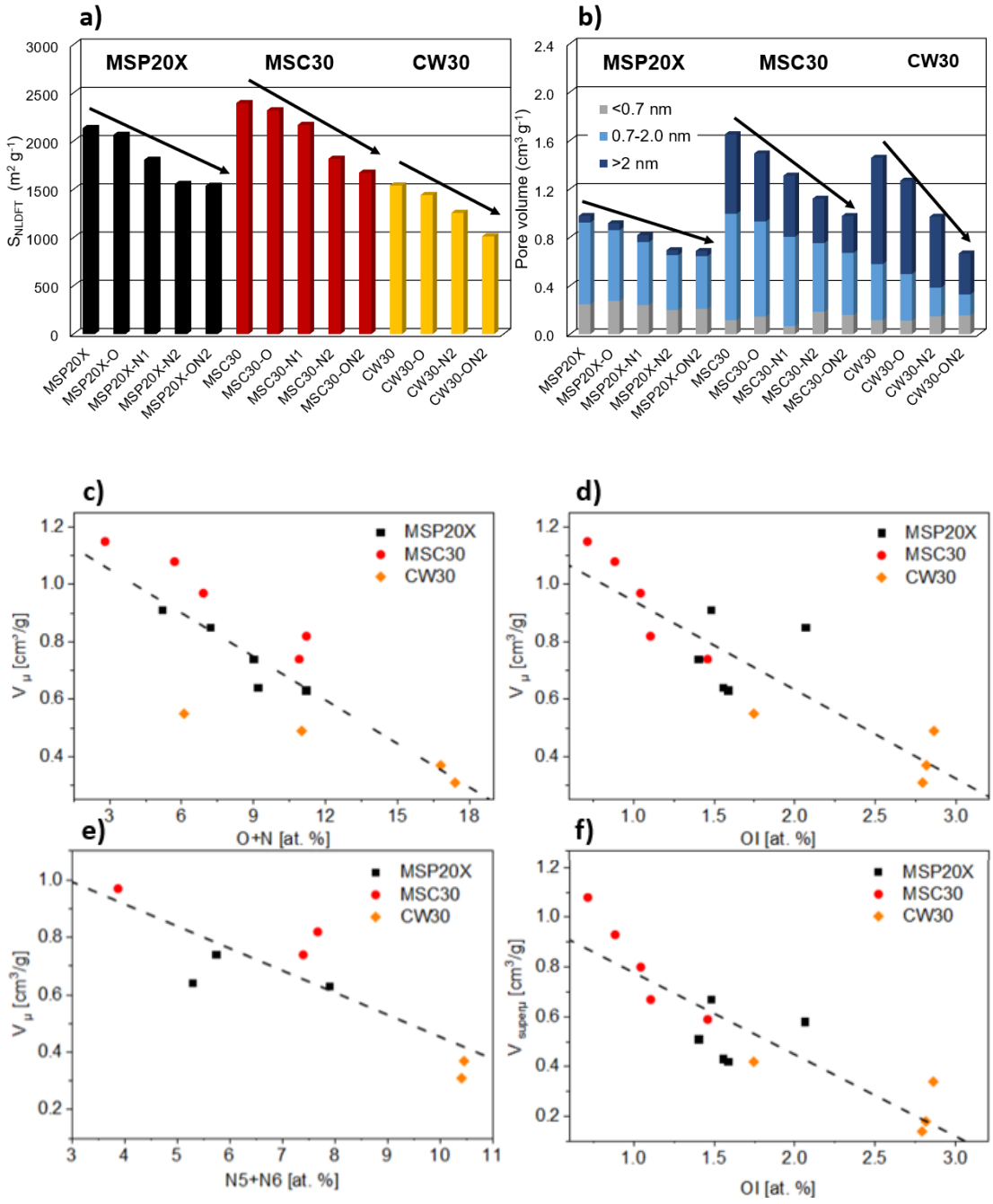


Figure 4. (a) $S_{NLDFT}$ specific surface area; and (b) total pore volume (micro- and mesopores) and their distribution in the different pore width ($w$) ranges, namely $w$< 0.7 nm, 0.7<$w$<2.0 nm, and > 2 nm <$w$< 50 nm. Evolution of micropore volume ($V_\mu$) as a function of (c) O+N, (d) OI and (e) N5+N6 content; and (f) evolution of super micropore ($V_{super\mu}$) as a function of OI content. The textural parameters were calculated using the 2D non-local density functional theory (2D-NLDFT).

The specific surface areas and total pore volumes exhibit a continuous decrease in the following order: *AC* > *AC-O* > *AC-N1* > *AC-N2* > *AC-ON2*. High values of $S_{NLDFT}$ surface area, between 1030 and 2520 $m^2$ $g^{-1}$, and total pore volume $V_{T,\,NLDFT}$ from 0.67 to 1.65 $cm^3$ $g^{-1}$, respectively, were found. Previous research has linked this reduction in surface area after urea treatment to the attachment of nitrogen groups to the edges of the carbon layers, which can partially impede pore accessibility[59,60].

The MSP20X series is predominantly characterized by a microporous structure, while the MSC30 and CW30 series feature a combination of micro- and meso-porosity. The CW30 series has a larger mesopore content, ranging from 30 to 40%. The calculated textural properties of all the materials studied are gathered in Table SI6. Cumulative pore volume graphs for the three series of ACs are also shown in the supplementary information, SI7.

Figures 4c, d, and e illustrate the changes in micropore volume as a function of total O+N content, quinonic oxygen content (OI), and combined pyrrolic (N5) and pyridinic (N6) nitrogen content (N5+N6). The reduction in micropore volume apparently correlates with O+N content, particularly in the case of OI. These findings suggest that the introduction of O+N resulted in pore narrowing. Figure 4f shows the decrease in supermicropore volume with increasing OI content values, in contrast to the ultra-microporous region (as seen in SI6). This behavior can be attributed to the limited ability of O and N atoms to penetrate the narrowest pores.

Chemical doping can lead to deformation of the carbon basal plane as well as direct steric hindrance. Surface groups like amines, amides, carboxyls and hydroxyls can occupy pore volume, while functional groups such as ethers, pyrroles and pyridines can distort the carbon structure based on simple geometrical considerations. Mostazo-López et al.[61] explained that such structures are frequently observed in O- and N-doped carbons. Therefore, induced steric hindrance and local deformation of the carbon structure led to pore narrowing and potential blocking [34].

### 3.3. $CO_2$ and $N_2$ adsorption at different temperatures

$CO_2$ adsorption isotherms, expressed in terms of mols per unit mass of adsorbent, were obtained for the three commercial ACs at temperatures of 273, 298 and 323 K, as shown in Figures 5a, b, and c. As expected for physisorption, there is a noticeable decrease in $CO_2$ uptake with increasing temperature. Similar trends were observed for chemically modified materials (see SI8, SI9, and SI10). Among the samples studied, MSC30 exhibited the highest $CO_2$ uptake at all three temperatures, up to 25 bar. This can be attributed to its more developed textural properties compared with other commercial ACs.

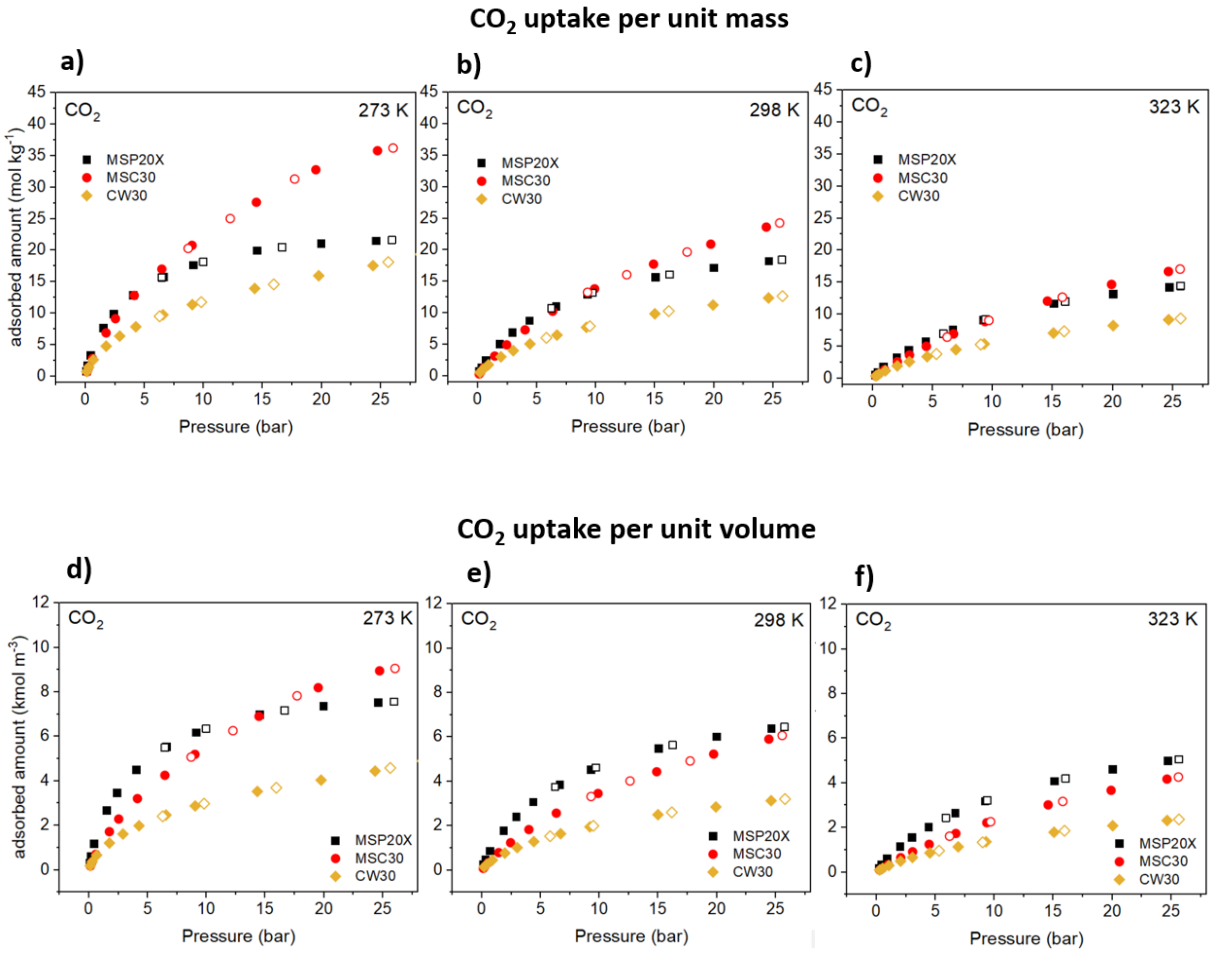


Figure 5. $CO_2$ isotherms per unit mass (mol $kg^{-1}$) for MSP20X, MSC30 and CW30 commercial ACs at (a) 273 K, (b) 298 K and (c) 323 K; and $CO_2$ isotherms (kmol $m^{-3}$) for the same ACs per unit volume at (d) 273 K, (e) 298 K and (f) 323 K. Solid symbols represent adsorption and empty symbols represent desorption.

However, if the tap density of the commercial ACs is considered when plotting the isotherms per unit volume, the order of $CO_2$ uptake is altered, as observed in Figures 5d, e, and f. The tap densities of the three ACs are: 350 kg $m^{-3}$ (MSP20X), 250 kg $m^{-3}$ (MSC30) and 253 kg $m^{-3}$ (CW30). Given the higher tap density of the MSP20X sample, the $CO_2$ uptake per unit volume exceeds that of the MSC30, particularly at temperatures of 298 K and 323 K. In the context of post-combustion $CO_2$ capture, where the use of fixed beds is common for $CO_2$ separation, the scenario involving 323 K and isotherms based on the volumetric capacities is considered more realistic for comparing adsorbents' capture performance. Consequently, based on this criterion, the MSP20X sample and its chemically modified counterparts have been selected for further analysis and discussion in this manuscript.

Figures 6a and b show $CO_2$ and $N_2$ adsorption-desorption isotherms at 323 K for the MSP20X series. The general trend is that $CO_2$ and $N_2$ uptakes decrease as the textural properties of the adsorbents are reduced, confirming that physisorption is the predominant adsorption mechanism. Comparison of

Figures 6a and b clearly shows that $CO_2$ is better adsorbed than $N_2$. This can be attributed to the higher quadrupole moment and polarizability of the $CO_2$ molecule, resulting in stronger interactions with the adsorbent surface during physisorption [62–64]. It is important to note that the results of this study are applicable in the context of doping ACs with heteroatoms. Previous studies[65–67] have suggested that ACs doped with heteroatoms, where doping takes place prior to activation, may exhibit higher $CO_2$ uptake per unit mass compared to the starting material. However, it remains difficult to distinguish the effect of textural properties from that of surface chemistry. To further investigate the relationship between textural properties, surface chemistry and their impact on $CO_2$ adsorption, a mathematical regression analysis was carried out in section 3.4.

The Sips adsorption model was used to analyze experimental $CO_2$ and $N_2$ adsorption data of commercial and chemically modified ACs. Figures 6c and d show the Sips model fits (represented by lines) for both the commercial AC MSP20X and the pre-oxidized, N-doped material MSP20X-ON2, allowing a direct comparison between a non-doped and a highly-doped material. Figures illustrating experimental isotherms and corresponding Sips model fits for the three series of materials can be found in SI8, SI9 and SI10. The values for the fitted parameters, together with the determination coefficients, are reported in SI11 for all samples. The determination coefficients obtained ranged from 0.99 to 1.0, indicating very good fits. This suggests that the parameters obtained can be used to calculate the isosteric heat of adsorption with the Clausius-Clapeyron approach.

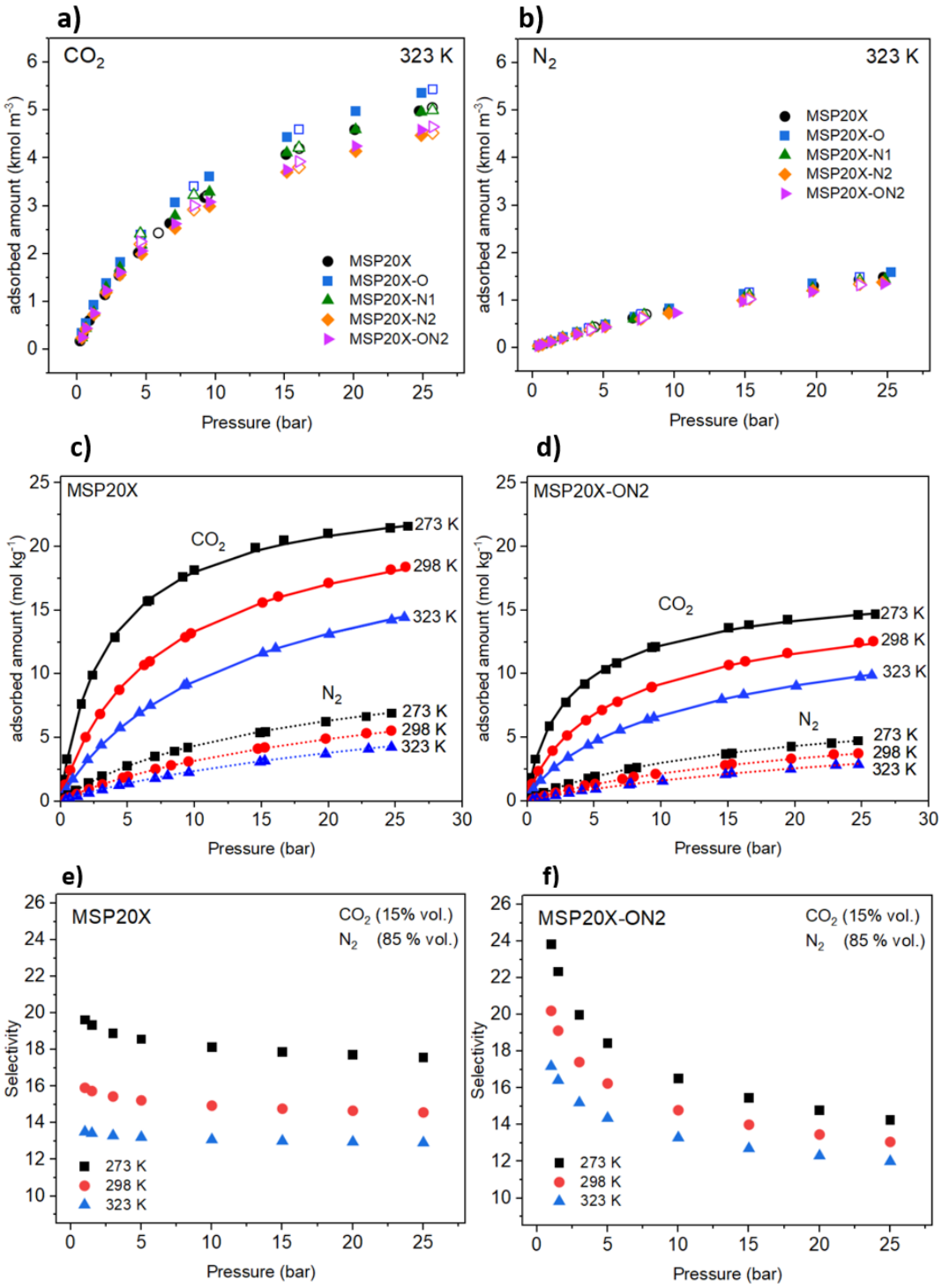


Figure 6. Experimental isotherms (kmol $m^{-3}$) of (a) $CO_2$ and (b) $N_2$ at 323 K for the AC series MSP20X. Solid symbols represent adsorption and empty symbols represent desorption. Experimental and fitted isotherms of $CO_2$ and $N_2$ of samples (c) MSP20X and (d) MSP20X-ON2 at 273, 298 and 323 K. Solid symbols represent experimental data and lines (straight and dotted) represent Sips model fits. $CO_2/N_2$ selectivity (15% vol. $CO_2$/85% vol. $N_2$) values for samples (e) MSP20X and (f) MSP20X-ON2 at 273, 298 and 323 K.

The selectivity of $CO_2$ capture over $N_2$ for the aforementioned samples was estimated using the well-known Ideal Adsorption Solution Theory (IAST) model as explained in SI1. Figures 6e and f show the selectivity of samples MSP20X and MSP20X-ON2 at different temperatures, specifically considering a dry post-combustion scenario with a binary mixture of $CO_2$ and $N_2$ in the flue gas, in which $CO_2$ accounts for 15% by volume. The results indicate that doping the material improves selectivity, particularly at lower pressures (below 5 bar). This suggests that the effect of heteroatoms is more advantageous at these pressure levels, where the energetic interaction between the material surface and heteroatoms is more pronounced. This observation is in line with the results in Figure 7a, where doped materials from the MSP20X series exhibit a higher isosteric heat of adsorption at low coverage.

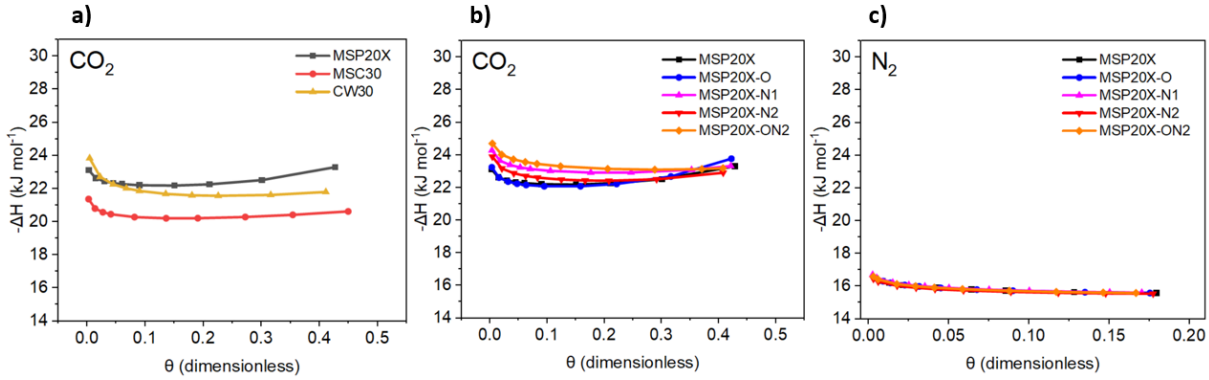


Figure 7. Isosteric heats of $CO_2$ adsorption on: (a) raw commercial ACs and (b) MSP20X series as a function of $CO_2$ fractional coverage (θ); and (c) Isosteric heats of $N_2$ adsorption on the MSP20X series as a function of $N_2$ fractional coverage.

Heat release during adsorption plays an essential role in a gas capture process, as it can influence adsorbent temperature, generate hot spots and impact adsorption kinetics[14]. The isosteric heats of adsorption were obtained from the fitted isotherms with Sips model at 273, 298, and 323 K in conjunction with the Clausius-Clapeyron equation (Equation 1) and they are plotted in Figure 7. Figure 7a shows a subtle increase in the isosteric heat of $CO_2$ adsorption for MSP20X with fractional $CO_2$ coverage ($\theta > 0.2$), in contrast to the decreasing trend shown by MSC30 and CW30. This behavior can be attributed to a predominance of intermolecular interactions between $CO_2$ molecules rather than surface-molecule interactions upon micropore filling completion[68,69]. Similar features in the isosteric heat of adsorption have been demonstrated for $CO_2$[70,71] as well as for other gases[72–74] and validated by

grand-canonical Monte Carlo modelling[75]. Figure 7b shows a decrease in isosteric heat of $CO_2$ adsorption as the amount adsorbed increases, particularly at low coverage for most of the doped ACs in the MSP20X family. This suggests stronger interactions between $CO_2$ and the surface at low pressure, indicating that the strongest adsorption sites are occupied first. Furthermore, the isosteric heat of $CO_2$ adsorption was slightly higher in the doped samples than in the untreated ACs, suggesting that heteroatom doping may increase energetic interactions at low surface coverage. A similar pattern was observed in the other two series of ACs (see SI12). The average heat of $CO_2$ adsorption, calculated for all materials (see SI13) considering coverage up to 0.5, was found to be well below 50 kJ $mol^{-1}$, confirming that the primary adsorption mechanism is based on physical interactions. Previous studies on ACs that have undergone chemical treatment have also reported similar average heats of adsorption (ranging from 20 to 30 kJ $mol^{-1}$)[14,77,78] to those presented in this study, ranging from 20 to 26 kJ $mol^{-1}$. These average heats of $CO_2$ adsorption fall within the range of the enthalpy of sublimation and vaporization of $CO_2$, which are 26.1 kJ $mol^{-1}$ and 16.7 kJ $mol^{-1}$,[79] respectively. This suggests that within the nanopores of ACs, the strong interaction forces present can cause $CO_2$ to exhibit a solid- or liquid-like behavior, depending on pore size and adsorption conditions. On the other hand, the isosteric heat for $N_2$ adsorption in the MSP20X series, as depicted in Figure 7c, remained almost constant, around 16 kJ $mol^{-1}$, across the coverage range evaluated, indicating the potential absence of intermolecular interactions and binding site heterogeneity[76]. Notably, isosteric heat values for adsorbed $N_2$ were observed to be lower than those for $CO_2$, aligning with the expected trend.

### 3.4. Effect of surface chemistry and textural properties on $CO_2$ uptake

Bearing in mind that the primary adsorption mechanism is based on physical interactions, and to evaluate the real effect of surface chemistry on $CO_2$ adsorption capacity, we normalized $CO_2$ uptakes with respect to $S_{NLDFT}$ specific surface area. Figures 8a and b illustrate $CO_2$ uptake per unit area as a function of O+N content for all ACs, pristine and doped, at different pressures of 0.25, 1.0, 7.0 and 25 bar at 273 and 323 K. Figure 8a shows a linear trend line with a positive slope up to 1 bar, meaning that higher O+N content results in improved $CO_2$ uptake per specific surface area at his pressure. However, the same figure shows that O+N content has no significant impact on $CO_2$ uptake at 5 bar. At higher

pressures, the slope of the linear trend line becomes negative, indicating that the presence of heteroatoms no longer offers any advantage for overall $CO_2$ uptake. Figure 8b shows the same data as Figure 8a when the adsorption temperature is raised to 323 K. At higher temperatures, the maximum pressure at which O+N content positively influences $CO_2$ uptake is higher, somewhere between 10 and 25 bar. Consequently, AC doping becomes more relevant at higher temperatures, demonstrating its efficacy over a wider pressure range.

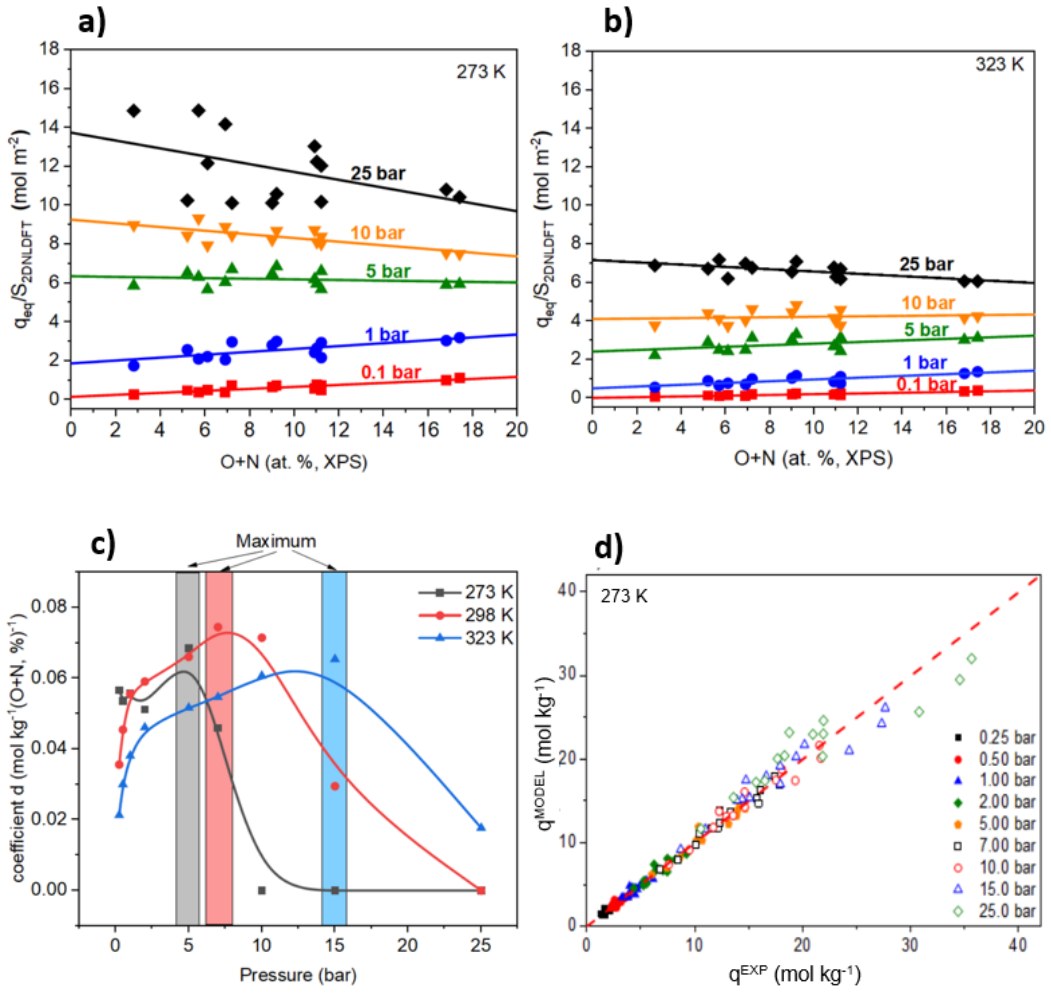


Figure 8. Relationship between O+N surface content and the $CO_2$ uptake per unit specific surface area $S_{2DNLDFT}$ at (a) 273 and (b) 323 K at different pressure levels for the ACs studied in this work. Solid lines represent the linear trend line for each selected pressure level: 0.1, 1, 5, 10 and 25 bar. (c) Coefficient *d* in Equation (2) versus pressure at different temperatures, and (d) comparison of experimental $CO_2$ uptake ($q^{EXP}$) versus predicted $CO_2$ uptake ($q^{MODEL}$) with Equation (2) at 273 K.

The mathematical regression analysis performed to better understand how textural properties and surface chemistry contribute to $CO_2$ adsorption was carried out as follows. Using the data given in the supplementary information, SI14, the adsorption capacity $q_{co_2}$ was fitted by Equation (2) and the

coefficient values for each temperature and pression can be found in the Supplementary Information, SI15. Figure 8c illustrates the variation of coefficient *d* in Equation (2) as a function of pressure. A consistent upward trend is observed up to a certain threshold, beyond which a noticeable decrease in coefficient *d* becomes evident. Additionally, the maximum value of parameter *d* shifts towards higher pressures as the isotherm temperature increases. This indicates that surface chemistry exerts a more prolonged influence over a broader pressure range at higher temperatures. Notably, at 323 K, the *d* coefficient does not approach a nearly negligible value as observed at the other two lower temperatures. In contrast, Figure 8d presents a comparison between experimental ($q^{EXP}$) and calculated ($q^{MODEL}$) $CO_2$ uptakes for different pressure levels and 273 K. The results indicate that the data predicted using Equation (2) are more accurate at lower pressures. Nonetheless, this mathematical approach proves to be a reliable method for estimating overall $CO_2$ uptake.

To highlight the impact of porosity and heteroatom content, we selected two samples, namely MSP20X and MSP20X-ON2. Sample MSP20X was chosen because it had not been chemically modified, yet had a surface heteroatom content of 5.2 at. % oxygen. On the other hand, sample MSP20X-ON2 underwent pre-oxidation and subsequent nitrogen-doping to further enhance its heteroatom content (11.2 at. % N+O). Based on the results presented in Figure 9, it can be observed that the influence of heteroatoms on $CO_2$ uptake becomes more prominent at higher pressure levels with increasing temperature. At the lowest temperature considered (298 K), neither sample exhibits a significant effect of heteroatoms in the 10-25 bar range. However, as temperature rises, the heteroatom effect becomes gradually evident at higher pressures, which is agreement with the results presented in Figure 8c. Additionally, it is worth noting that the doping effect is more pronounced in MSP20X-ON2 than in MSP20X, indicating that a higher overall heteroatom content may reinforce the significance of surface chemistry in $CO_2$ uptake. Nevertheless, Figure 9 shows that textural properties play a more important role in $CO_2$ adsorption, since higher uptakes were obtained with the pristine AC.

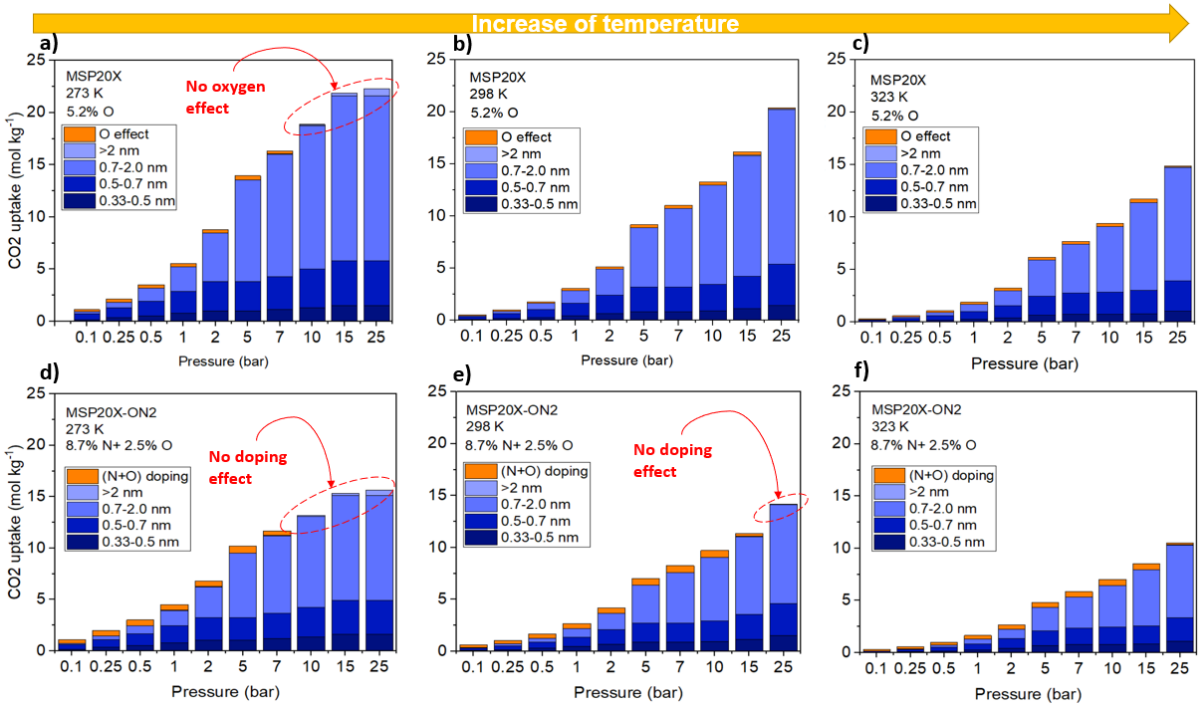


Figure 9. Influence of pore size distribution and surface heteroatoms on $CO_2$ uptake for samples MSP20X at (a) 273 K, (b) 298 K and (c) 323 K, and for MSP20X-ON2 at (d) 273 K, (e) 298 K and (f) 323 K.

### 3.5. Adsorbent tap density and breakthrough curve simulation

Adsorbent density plays a crucial role in the design of an adsorption process, more specifically for the cases where fixed-beds are used. Assuming constant adsorption capacity per unit mass, a material with a higher packing density will result in more effective adsorption per unit volume. Consequently, the denser material will result in lower vessel costs and occupy less space in an industrial facility. Figure 10b provides a visual representation of the relationship between tap density and variation in N+O content in the MSP20X series.

To better understand the impact of the adsorption parameters analyzed, a simulation of the adsorption breakthrough curves was carried out for the MSP20X series under different conditions, according to the scheme described in Figure 10a. Figure 10a also presents the selected parameters used to solve the model, as described in the experimental section. Figure 10c shows the breakthrough simulation at 5 bar in an ideal scenario, where all materials have an isosteric heat of adsorption of zero and have the same bulk density. However, when the simulation was run with the actual tap density, the dynamics changed as shown in Fig. 10d. Increasing the tap density led to a prolonged breakthrough time

for MSP20X-O. The performance of the other N- and O-N-doped materials improved only slightly, with breakthrough times very close to those of MSP20X.

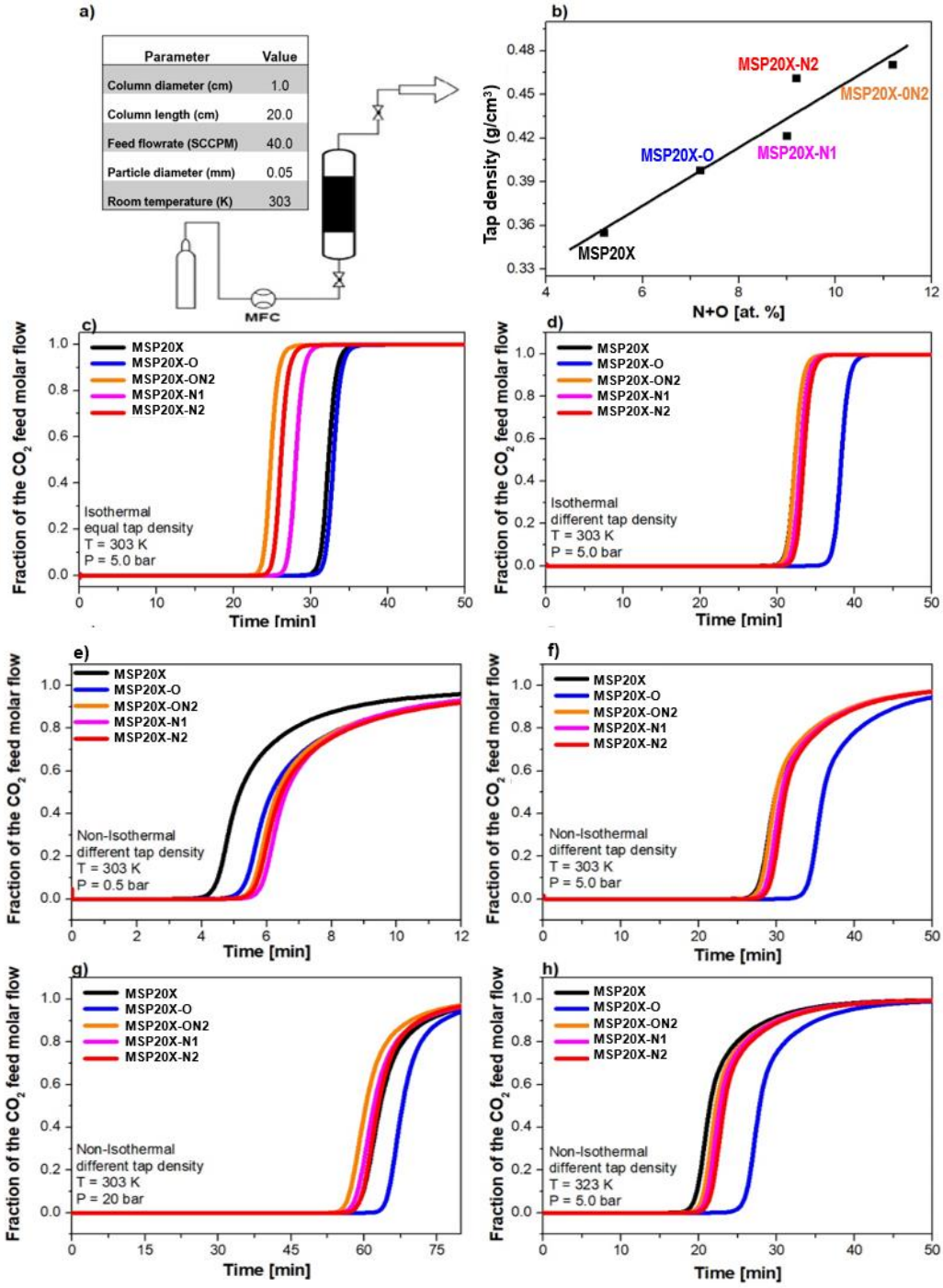


Figure 10. (a) Schematic of simulated fixed-bed system. For the MSP20X series: (b) tap density as a function of O+N content; (c) isothermal breakthrough simulation at 303 K and 5 bar, considering all tap densities equal to that of the raw AC; (d) isothermal breakthrough simulation at 303 K and 5 bar considering the tap density of the ACs; (e) non-isothermal, adiabatic breakthrough simulation at 303 K and 0.5 bar; (f) non-isothermal, adiabatic breakthrough simulation at 303 K and 5 bar; (g) non-isothermal, adiabatic breakthrough simulation at 303 K and 20 bar; (h) non-isothermal, adiabatic breakthrough simulation at 323 K and 5 bar.

Three simulations were carried out to analyze a non-isothermal adsorption process under the following conditions: process temperature of 303 K and pressures of 0.5 bar (Figure 10e), 5 bar (Figure 10f), and 20 bar (Figure 10g). At a pressure of 0.5 bar, the doped materials exhibited a higher affinity for $CO_2$, as evidenced by the shorter breakthrough time for the raw MSP20X compared with its doped counterparts. At 5 bar and 303 K, MSP20X-O emerged as the best performing sample in terms of $CO_2$ uptake. Even when the temperature was increased to 323 K, as shown in Figure 10h, the trend in results remained the same as at 303 K. The superior performance of MSP20X-O can be attributed to a balance between $CO_2$ adsorption capacity, essentially governed by textural properties, and tap density. This undoubtedly underlines the crucial importance of volumetric adsorption capacity, and the need to present it alongside specific adsorption capacities in reports on the performance of newly developed materials.

Comparing the breakthrough at temperatures of 303 K (Figure 10g) and 323 K (Figure 10h), it is evident that an increase in temperature reduces the performance of MSP20X compared with doped materials, confirming the greater influence of surface chemistry at higher temperatures. Overall, the results suggest that a particular degree of doping plays a more important role in improving adsorption performance, especially when the pressure is below 5 bar, and preferably at elevated temperatures such as 323 K. Conversely, under conditions of higher pressures and lower temperatures than those mentioned above, the impact of surface chemistry is relatively low.

## 4. Conclusion

This study unequivocally demonstrates that up to pressures of 25 bar and in the temperature range 273-323 K, textural properties take precedence in determining $CO_2$ uptake by carbon materials. N-O-doping primarily affects larger pores, resulting in reduced textural properties and subsequent adsorption. Nonetheless, it improved $CO_2/N_2$ selectivity, particularly up to 5 bar and in the temperature range 273-323 K. Therefore, we can conclude that heteroatom doping is not always the best strategy for enhancing $CO_2$ adsorption, which was corroborated mathematically by considering the pore size distribution and the presence of N+O heteroatoms. Doping increased the isosteric heat of adsorption for fractional coverage below 0.2, but the average isosteric heat of adsorption remained below 50 kJ $mol^{-1}$, consistent

with physical adsorption processes. Furthermore, this study underlines the importance of a crucial parameter that should be systematically taken into account for practical applications: the tap density of the adsorbent. This parameter has a significant influence on breakthrough performance in fixed-bed columns, but is not systematically reported in studies focusing on the development of new adsorbents.

**Acknowledgements:** TALiSMAN and TALiSMAN2 projects funded by the European Regional Development Fund (ERDF) are gratefully acknowledged. This work has been partially supported by project no ANR-22-PESP-0007 from the Agence Nationale de la Recherche (France 2030).

## References


(1) Singh, V. K.; Anil Kumar, E. Measurement and Analysis of Adsorption Isotherms of CO2 on Activated Carbon. *Appl. Therm. Eng.* **2016**, *97*, 77–86. https://doi.org/10.1016/j.applthermaleng.2015.10.052.

(2) Han, J.; Zhang, L.; Zhao, B.; Qin, L.; Wang, Y.; Xing, F. The N-Doped Activated Carbon Derived from Sugarcane Bagasse for CO2 Adsorption. *Ind. Crops Prod.* **2019**, *128*, 290–297. https://doi.org/10.1016/j.indcrop.2018.11.028.

(3) Florides, G. A.; Christodoulides, P. Global Warming and Carbon Dioxide through Sciences. *Environ. Int.* **2009**, *35* (2), 390–401. https://doi.org/10.1016/j.envint.2008.07.007.

(4) Canevesi, R. L. S.; Andreassen, K. A.; Silva, E. A.; Borba, C. E.; Grande, C. A. Evaluation of Simplified Pressure Swing Adsorption Cycles for Bio-Methane Production. *Adsorption* **2019**, *0* (0), 0. https://doi.org/10.1007/s10450-019-00049-x.

(5) Alami, A. H.; Abu Hawili, A.; Tawalbeh, M.; Hasan, R.; Al Mahmoud, L.; Chibib, S.; Mahmood, A.; Aokal, K.; Rattanapanya, P. Materials and Logistics for Carbon Dioxide Capture, Storage and Utilization. *Sci. Total Environ.* **2020**, *717*, 137221. https://doi.org/10.1016/j.scitotenv.2020.137221.

(6) Liang, Z.; Fu, K.; Idem, R.; Tontiwachwuthikul, P. Review on Current Advances, Future Challenges and Consideration Issues for Post-Combustion CO2 Capture Using Amine-Based Absorbents. *Chin. J. Chem. Eng.* **2016**, *24* (2), 278–288. https://doi.org/10.1016/j.cjche.2015.06.013.

(7) Samanta, A.; Zhao, A.; Shimizu, G. K. H.; Sarkar, P.; Gupta, R. Post-Combustion CO2 Capture Using Solid Sorbents: A Review. *Ind. Eng. Chem. Res.* **2011**, *51* (4), 1438–1463. https://doi.org/10.1021/ie200686q.

(8) Nie, L.; Mu, Y.; Jin, J.; Chen, J.; Mi, J. Recent Developments and Consideration Issues in Solid Adsorbents for CO2 Capture from Flue Gas. *Chin. J. Chem. Eng.* **2018**, *26* (11), 2303–2317. https://doi.org/10.1016/j.cjche.2018.07.012.

(9) Leung, D. Y. C.; Caramanna, G.; Maroto-Valer, M. M. An Overview of Current Status of Carbon Dioxide Capture and Storage Technologies. *Renew. Sustain. Energy Rev.* **2014**, *39*, 426–443. https://doi.org/10.1016/j.rser.2014.07.093.

(10) Aminu, M. D.; Nabavi, S. A.; Rochelle, C. A.; Manovic, V. A Review of Developments in Carbon Dioxide Storage. *Appl. Energy* **2017**, *208*, 1389–1419. https://doi.org/10.1016/j.apenergy.2017.09.015.

(11) Olajire, A. A. CO2 Capture and Separation Technologies for End-of-Pipe Applications – A Review. *Energy* **2010**, *35* (6), 2610–2628. https://doi.org/10.1016/j.energy.2010.02.030.

(12) Mondal, M. K.; Balsora, H. K.; Varshney, P. Progress and Trends in CO2 Capture/Separation Technologies: A Review. *Energy* **2012**, *46* (1), 431–441. https://doi.org/10.1016/j.energy.2012.08.006.

(13) Grande, C. A.; Kvamsdal, H.; Mondino, G.; Blom, R. Development of Moving Bed Temperature Swing Adsorption (MBTSA) Process for Post-Combustion CO 2 Capture: Initial Benchmarking in a NGCC Context. *Energy Procedia* **2017**, *114*, 2203–2210. https://doi.org/10.1016/j.egypro.2017.03.1357.

(14) Park, Y.; Moon, D.-K.; Kim, Y.-H.; Ahn, H.; Lee, C.-H. Adsorption Isotherms of CO2, CO, N2, CH4, Ar and H2 on Activated Carbon and Zeolite LiX up to 1.0 MPa. *Adsorption* **2014**, *20* (4), 631–647. https://doi.org/10.1007/s10450-014-9608-x.

(15) Liang, Z.; Marshall, M.; Chaffee, A. L. CO $_2$ Adsorption-Based Separation by Metal Organic Framework (Cu-BTC) versus Zeolite (13X). *Energy Fuels* **2009**, *23* (5), 2785–2789. https://doi.org/10.1021/ef800938e.

(16) Modak, A.; Jana, S. Advancement in Porous Adsorbents for Post-Combustion CO2 Capture. *Microporous Mesoporous Mater.* **2019**, *276*, 107–132. https://doi.org/10.1016/j.micromeso.2018.09.018.
(17) Chen, J.; Loo, L. S.; Wang, K. High-Pressure CO $_2$ Adsorption on a Polymer-Derived Carbon Molecular Sieve. *J. Chem. Eng. Data* **2008**, *53* (1), 2–4. https://doi.org/10.1021/je700178y.
(18) Guo, B.; Chang, L.; Xie, K. Adsorption of Carbon Dioxide on Activated Carbon. *J. Nat. Gas Chem.* **2006**, *15* (3), 223–229. https://doi.org/10.1016/S1003-9953(06)60030-3.
(19) Casco, M. E.; Martínez-Escandell, M.; Silvestre-Albero, J.; Rodríguez-Reinoso, F. Effect of the Porous Structure in Carbon Materials for CO2 Capture at Atmospheric and High-Pressure. *Carbon* **2014**, *67*, 230–235. https://doi.org/10.1016/j.carbon.2013.09.086.
(20) García-Díez, E.; Schaefer, S.; Sanchez-Sanchez, A.; Celzard, A.; Fierro, V.; Maroto-Valer, M. M.; García, S. Novel Porous Carbons Derived from Coal Tar Rejects: Assessment of the Role of Pore Texture in CO2 Capture under Realistic Postcombustion Operating Temperatures. *ACS Appl. Mater. Interfaces* **2019**, *11* (40), 36789–36799. https://doi.org/10.1021/acsami.9b13247.
(21) Jiménez, V.; Sánchez, P.; Valverde, J. L.; Romero, A. Effect of the Nature the Carbon Precursor on the Physico-Chemical Characteristics of the Resulting Activated Carbon Materials. *Mater. Chem. Phys.* **2010**, *124* (1), 223–233. https://doi.org/10.1016/j.matchemphys.2010.06.023.
(22) Muriithi, G. N.; Petrik, L. F.; Doucet, F. J. Synthesis, Characterisation and CO2 Adsorption Potential of NaA and NaX Zeolites and Hydrotalcite Obtained from the Same Coal Fly Ash. *J. CO2 Util.* **2020**, *36*, 220–230. https://doi.org/10.1016/j.jcou.2019.11.016.
(23) Lyu, C.; Hao, S.-Q.; Sun, Q. Experiment Study on the Correlation between the CO2 Adsorption Capacity and Electrical Resistivity of Coal with Temperature Effect. *Greenh. Gases Sci. Technol.* **2019**, *9* (5), 924–933. https://doi.org/10.1002/ghg.1910.
(24) Schaefer, S.; Jeder, A.; Sdanghi, G.; Gadonneix, P.; Abdedayem, A.; Izquierdo, M. T.; Maranzana, G.; Ouederni, A.; Celzard, A.; Fierro, V. Oxygen-Promoted Hydrogen Adsorption on Activated and Hybrid Carbon Materials. *Int. J. Hydrog. Energy* **2020**. https://doi.org/10.1016/j.ijhydene.2020.08.114.
(25) Castro-Gutiérrez, J.; Celzard, A.; Fierro, V. Energy Storage in Supercapacitors: Focus on Tannin-Derived Carbon Electrodes. *Front. Mater.* **2020**, *7*. https://doi.org/10.3389/fmats.2020.00217.
(26) Castro-Gutiérrez, J.; Palaimiene, E.; Macutkevic, J.; Banys, J.; Kuzhir, P.; Schaefer, S.; Fierro, V.; Celzard, A. Electromagnetic Properties of Carbon Gels. *Materials* **2019**, *12* (24), 4143. https://doi.org/10.3390/ma12244143.
(27) Bai, F.; Xia, Y.; Chen, B.; Su, H.; Zhu, Y. Preparation and Carbon Dioxide Uptake Capacity of N-Doped Porous Carbon Materials Derived from Direct Carbonization of Zeolitic Imidazolate Framework. *Carbon* **2014**, *79*, 213–226. https://doi.org/10.1016/j.carbon.2014.07.062.
(28) Shi, W.; Wang, R.; Liu, H.; Chang, B.; Yang, B.; Zhang, Z. Biowaste-Derived 3D Honeycomb-like N and S Dual-Doped Hierarchically Porous Carbons for High-Efficient CO 2 Capture. *RSC Adv.* **2019**, *9* (40), 23241–23253. https://doi.org/10.1039/C9RA03659H.
(29) Braghiroli, F. L.; Fierro, V.; Izquierdo, M. T.; Parmentier, J.; Pizzi, A.; Delmotte, L.; Fioux, P.; Celzard, A. High Surface – Highly N-Doped Carbons from Hydrothermally Treated Tannin. *Ind. Crops Prod.* **2015**, *66*, 282–290. https://doi.org/10.1016/j.indcrop.2014.11.022.
(30) Wang, L.; Rao, L.; Xia, B.; Wang, L.; Yue, L.; Liang, Y.; DaCosta, H.; Hu, X. Highly Efficient CO2 Adsorption by Nitrogen-Doped Porous Carbons Synthesized with Low-

Temperature Sodium Amide Activation. *Carbon* **2018**, *130*, 31–40. https://doi.org/10.1016/j.carbon.2018.01.003.
(31) Lee, S.-Y.; Park, S.-J. Determination of the Optimal Pore Size for Improved CO2 Adsorption in Activated Carbon Fibers. *J. Colloid Interface Sci.* **2013**, *389* (1), 230–235. https://doi.org/10.1016/j.jcis.2012.09.018.
(32) Sevilla, M.; Fuertes, A. B. Sustainable Porous Carbons with a Superior Performance for CO2 Capture. *Energy Env. Sci* **2011**, *4* (5), 1765–1771. https://doi.org/10.1039/C0EE00784F.
(33) Marco-Lozar, J. P.; Kunowsky, M.; Suárez-García, F.; Linares-Solano, A. Sorbent Design for CO2 Capture under Different Flue Gas Conditions. *Carbon* **2014**, *72*, 125–134. https://doi.org/10.1016/j.carbon.2014.01.064.
(34) Canevesi, R. L. S.; Schaefer, S.; Izquierdo, M. T.; Celzard, A.; Fierro, V. Roles of Surface Chemistry and Texture of Nanoporous Activated Carbons in CO 2 Capture. *ACS Appl. Nano Mater.* **2022**, *5* (3), 3843–3854. https://doi.org/10.1021/acsanm.1c04474.
(35) García-Díez, E.; Schaefer, S.; Sanchez-Sanchez, A.; Celzard, A.; Fierro, V.; Maroto-Valer, M. M.; García, S. Novel Porous Carbons Derived from Coal Tar Rejects: Assessment of the Role of Pore Texture in CO2 Capture under Realistic Postcombustion Operating Temperatures. *ACS Appl. Mater. Interfaces* **2019**, *11* (40), 36789–36799. https://doi.org/10.1021/acsami.9b13247.
(36) Saning, A.; Dubadi, R.; Chuenchom, L.; Dechtrirat, D.; Jaroniec, M. Microporous Carbons Obtained via Solvent-Free Mechanochemical Processing, Carbonization and Activation with Potassium Citrate and Zinc Chloride for CO2 Adsorption. *Separations* **2023**, *10* (5). https://doi.org/10.3390/separations10050304.
(37) Dubadi, R.; Jaroniec, M. One-Pot Mechanochemical Synthesis of Carbons with High Microporosity and Ordered Mesopores for CO2 Uptake at Ambient Conditions. *Nanomaterials* **2023**, *13* (15). https://doi.org/10.3390/nano13152262.
(38) Gunathilake, C.; Dassanayake, R. S.; Kalpage, C. S.; Jaroniec, M. Development of Alumina–Mesoporous Organosilica Hybrid Materials for Carbon Dioxide Adsorption at 25 °C. *Materials* **2018**, *11* (11). https://doi.org/10.3390/ma11112301.
(39) Dassanayake, A. C.; Jaroniec, M. Activated Polypyrrole-Derived Carbon Spheres for Superior CO2 Uptake at Ambient Conditions. *Colloids Surf. Physicochem. Eng. Asp.* **2018**, *549*, 147–154. https://doi.org/10.1016/j.colsurfa.2018.04.002.
(40) Choma, J.; Osuchowski, L.; Marszewski, M.; Dziura, A.; Jaroniec, M. Developing Microporosity in Kevlar®-Derived Carbon Fibers by CO2 Activation for CO2 Adsorption. *J. CO2 Util.* **2016**, *16*, 17–22. https://doi.org/10.1016/j.jcou.2016.05.004.
(41) Kiełbasa, K.; Kamińska, A.; Niedoba, O.; Michalkiewicz, B. CO2 Adsorption on Activated Carbons Prepared from Molasses: A Comparison of Two and Three Parametric Models. *Materials* **2021**, *14* (23). https://doi.org/10.3390/ma14237458.
(42) Siemak, J.; Michalkiewicz, B. Enhancement of CO2 Adsorption on Activated Carbons Produced from Avocado Seeds by Combined Solvothermal Carbonization and Thermal KOH Activation. *Environ. Sci. Pollut. Res.* **2023**. https://doi.org/10.1007/s11356-023-28638-y.
(43) Bae, T. H.; Hudson, M. R.; Mason, J. A.; Queen, W. L.; Dutton, J. J.; Sumida, K.; Micklash, K. J.; Kaye, S. S.; Brown, C. M.; Long, J. R. Evaluation of Cation-Exchanged ZeoliteAdsorbents for Post-Combustion Carbon Dioxide Capture. *Energy Env. Sci* **2013**, *6*, 128.
(44) Bhown, A. S.; Freeman, B. C. Analysis and Status of Post-Combustion Carbon Dioxide Capture Technologies. *Env. Sci Technol* **2011**, *45* (20), 8624–8632. https://doi.org/10.1021/es104291d.

(45) Jagiello, J.; Kenvin, J.; Ania, C. O.; Parra, J. B.; Celzard, A.; Fierro, V. Exploiting the Adsorption of Simple Gases O2 and H2 with Minimal Quadrupole Moments for the Dual Gas Characterization of Nanoporous Carbons Using 2D-NLDFT Models. *Carbon* **2020**, *160*, 164–175. https://doi.org/10.1016/j.carbon.2020.01.013.
(46) Sips, R. On the Structure of a Catalyst Surface. *J. Chem. Phys.* **1948**, *16* (5), 490–495. https://doi.org/10.1063/1.1746922.
(47) Canevesi, R. L. S.; Andreassen, K. A.; Silva, E. A.; Borba, C. E.; Grande, C. A. Evaluation of Simplified Pressure Swing Adsorption Cycles for Bio-Methane Production. *Adsorption* **2019**, *25* (4), 783–793. https://doi.org/10.1007/s10450-019-00049-x.
(48) Canevesi, R. L. S.; Andreassen, K. A.; da Silva, E. A.; Borba, C. E.; Grande, C. A. Pressure Swing Adsorption for Biogas Upgrading with Carbon Molecular Sieve. *Ind. Eng. Chem. Res.* **2018**, *57* (23), 8057–8067. https://doi.org/10.1021/acs.iecr.8b00996.
(49) Greco, G.; Canevesi, R. L. S.; Di Stasi, C.; Celzard, A.; Fierro, V.; Manyà, J. J. Biomass-Derived Carbons Physically Activated in One or Two Steps for CH4/CO2 Separation. *Renew. Energy* **2022**, *191*, 122–133. https://doi.org/10.1016/j.renene.2022.04.035.
(50) Hulicova-Jurcakova, D.; Seredych, M.; Lu, G. Q.; Bandosz, T. J. Combined Effect of Nitrogen- and Oxygen-Containing Functional Groups of Microporous Activated Carbon on Its Electrochemical Performance in Supercapacitors. *Adv. Funct. Mater.* **2009**, *19* (3), 438–447. https://doi.org/10.1002/adfm.200801236.
(51) Mostazo-López, M. J.; Ruiz-Rosas, R.; Morallón, E.; Cazorla-Amorós, D. Generation of Nitrogen Functionalities on Activated Carbons by Amidation Reactions and Hofmann Rearrangement: Chemical and Electrochemical Characterization. *Carbon* **2015**, *91*, 252–265. https://doi.org/10.1016/j.carbon.2015.04.089.
(52) Sanchez-Sanchez, A.; Braghiroli, F. L.; Izquierdo, M. T.; Parmentier, J.; Celzard, A.; Fierro, V. Synthesis and Properties of Carbon Microspheres Based on Tannin–Sucrose Mixtures Treated in Hydrothermal Conditions. *Ind. Crops Prod.* **2020**, *154*, 112564. https://doi.org/10.1016/j.indcrop.2020.112564.
(53) Dongil, A. B.; Bachiller-Baeza, B.; Guerrero-Ruiz, A.; Rodríguez-Ramos, I.; Martínez-Alonso, A.; Tascón, J. M. D. Surface Chemical Modifications Induced on High Surface Area Graphite and Carbon Nanofibers Using Different Oxidation and Functionalization Treatments. *J. Colloid Interface Sci.* **2011**, *355* (1), 179–189. https://doi.org/10.1016/j.jcis.2010.11.066.
(54) Gokce, Y.; Aktas, Z. Nitric Acid Modification of Activated Carbon Produced from Waste Tea and Adsorption of Methylene Blue and Phenol. *Appl. Surf. Sci.* **2014**, *313*, 352–359. https://doi.org/10.1016/j.apsusc.2014.05.214.
(55) Jaramillo, J.; Álvarez, P. M.; Gómez-Serrano, V. Oxidation of Activated Carbon by Dry and Wet Methods. *Fuel Process. Technol.* **2010**, *91* (11), 1768–1775. https://doi.org/10.1016/j.fuproc.2010.07.018.
(56) Sanchez-Sanchez, A.; Izquierdo, M. T.; Mathieu, S.; Medjahdi, G.; Fierro, V.; Celzard, A. Activated Carbon Xerogels Derived from Phenolic Oil: Basic Catalysis Synthesis and Electrochemical Performances. *Fuel Process. Technol.* **2020**, *205*, 106427. https://doi.org/10.1016/j.fuproc.2020.106427.
(57) Weidenthaler, C.; Lu, A.-H.; Schmidt, W.; Schüth, F. X-Ray Photoelectron Spectroscopic Studies of PAN-Based Ordered Mesoporous Carbons (OMC). *Microporous Mesoporous Mater.* **2006**, *88* (1), 238–243. https://doi.org/10.1016/j.micromeso.2005.09.015.
(58) Thommes, M.; Kaneko, K.; Neimark, A. V.; Olivier, J. P.; Rodriguez-Reinoso, F.; Rouquerol, J.; Sing, K. S. W. Physisorption of Gases, with Special Reference to the Evaluation of Surface Area and Pore Size Distribution (IUPAC Technical Report). *Pure Appl. Chem.* **2015**, *87* (9–10). https://doi.org/10.1515/pac-2014-1117.

(59) Bashkova, S.; Bandosz, T. J. The Effects of Urea Modification and Heat Treatment on the Process of NO2 Removal by Wood-Based Activated Carbon. *J. Colloid Interface Sci.* **2009**, *333* (1), 97–103. https://doi.org/10.1016/j.jcis.2009.01.052.
(60) Arenillas, A.; Rubiera, F.; Parra, J. B.; Ania, C. O.; Pis, J. J. Surface Modification of Low Cost Carbons for Their Application in the Environmental Protection. *Appl. Surf. Sci.* **2005**, *252* (3), 619–624. https://doi.org/10.1016/j.apsusc.2005.02.076.
(61) Mostazo-López, M. J.; Salinas-Torres, D.; Ruiz-Rosas, R.; Morallón, E.; Cazorla-Amorós, D. Nitrogen-Doped Superporous Activated Carbons as Electrocatalysts for the Oxygen Reduction Reaction. *Materials* **2019**, *12* (8). https://doi.org/10.3390/ma12081346.
(62) Ruthven, D. M. *Principles of Adsorption and Adsorption Processes*; Wiley: New York, 1984.
(63) Shang, J.; Li, G.; Singh, R.; Xiao, P.; Liu, J. Z.; Webley, P. A. Determination of Composition Range for "Molecular Trapdoor" Effect in Chabazite Zeolite. *J. Phys. Chem. C* **2013**, *117* (24), 12841–12847. https://doi.org/10.1021/jp4015146.
(64) Dindi, A.; Quang, D. V.; Vega, L. F.; Nashef, E.; Abu-Zahra, M. R. M. Applications of Fly Ash for CO2 Capture, Utilization, and Storage. *J. CO2 Util.* **2019**, *29*, 82–102. https://doi.org/10.1016/j.jcou.2018.11.011.
(65) Bai, J.; Huang, J.; Yu, Q.; Demir, M.; Kilic, M.; Altay, B. N.; Hu, X.; Wang, L. N-Doped Porous Carbon Derived from Macadamia Nut Shell for CO2 Adsorption. *Fuel Process. Technol.* **2023**, *249*, 107854. https://doi.org/10.1016/j.fuproc.2023.107854.
(66) Shao, J.; Ma, C.; Zhao, J.; Wang, L.; Hu, X. Effective Nitrogen and Sulfur Co-Doped Porous Carbonaceous CO2 Adsorbents Derived from Amino Acid. *Colloids Surf. Physicochem. Eng. Asp.* **2022**, *632*, 127750. https://doi.org/10.1016/j.colsurfa.2021.127750.
(67) Ma, C.; Lu, T.; Shao, J.; Huang, J.; Hu, X.; Wang, L. Biomass Derived Nitrogen and Sulfur Co-Doped Porous Carbons for Efficient CO2 Adsorption. *Sep. Purif. Technol.* **2022**, *281*, 119899. https://doi.org/10.1016/j.seppur.2021.119899.
(68) Juliš, J. Differential Heats of Adsorption. *Chem. Pap.* **1975**, *29* (5), 653–659.
(69) Farmahini, A. H.; Bhatia, S. K. Differences in the Adsorption and Diffusion Behaviour of Water and Non-Polar Gases in Nanoporous Carbon: Role of Cooperative Effects of Pore Confinement and Hydrogen Bonding. *Mol. Simul.* **2015**, *41* (5–6), 432–445. https://doi.org/10.1080/08927022.2014.976640.
(70) Furmaniak, S.; Terzyk, A. P.; Gauden, P. A.; Harris, P. J. F.; Kowalczyk, P. The Influence of Carbon Surface Oxygen Groups on Dubinin–Astakhov Equation Parameters Calculated from CO2adsorption Isotherm. *J. Phys. Condens. Matter* **2010**, *22* (8), 085003. https://doi.org/10.1088/0953-8984/22/8/085003.
(71) Murialdo, M.; Ahn, C. C.; Fultz, B. A Thermodynamic Investigation of Adsorbate-Adsorbate Interactions of Carbon Dioxide on Nanostructured Carbons. *AIChE J.* **2018**, *64* (3), 1026–1033. https://doi.org/10.1002/aic.15996.
(72) Farmahini, A. H.; Bhatia, S. K. Differences in the Adsorption and Diffusion Behaviour of Water and Non-Polar Gases in Nanoporous Carbon: Role of Cooperative Effects of Pore Confinement and Hydrogen Bonding. *Mol. Simul.* **2015**, *41* (5–6), 432–445. https://doi.org/10.1080/08927022.2014.976640.
(73) Murialdo, M.; Stadie, N. P.; Ahn, C. C.; Fultz, B. Observation and Investigation of Increasing Isosteric Heat of Adsorption of Ethane on Zeolite-Templated Carbon. *J. Phys. Chem. C* **2015**, *119* (2), 944–950. https://doi.org/10.1021/jp510991y.
(74) Stadie, N. P.; Murialdo, M.; Ahn, C. C.; Fultz, B. Anomalous Isosteric Enthalpy of Adsorption of Methane on Zeolite-Templated Carbon. *J. Am. Chem. Soc.* **2013**, *135* (3), 990–993. https://doi.org/10.1021/ja311415m.

(75) Torres-Knoop, A.; Poursaeidesfahani, A.; Vlugt, T. J. H.; Dubbeldam, D. Behavior of the Enthalpy of Adsorption in Nanoporous Materials Close to Saturation Conditions. *J. Chem. Theory Comput.* **2017**, *13* (7), 3326–3339. https://doi.org/10.1021/acs.jctc.6b01193.

(76) Madani, S. H.; Sedghi, S.; Biggs, M. J.; Pendleton, P. Analysis of Adsorbate–Adsorbate and Adsorbate–Adsorbent Interactions to Decode Isosteric Heats of Gas Adsorption. *ChemPhysChem* **2015**, *16* (18), 3797–3805. https://doi.org/10.1002/cphc.201500881.

(77) Rao, L.; Ma, R.; Liu, S.; Wang, L.; Wu, Z.; Yang, J.; Hu, X. Nitrogen Enriched Porous Carbons from D-Glucose with Excellent CO2 Capture Performance. *Chem. Eng. J.* **2019**, *362*, 794–801. https://doi.org/10.1016/j.cej.2019.01.093.

(78) Chen, J.; Yang, J.; Hu, G.; Hu, X.; Li, Z.; Shen, S.; Radosz, M.; Fan, M. Enhanced $CO_2$ Capture Capacity of Nitrogen-Doped Biomass-Derived Porous Carbons. *ACS Sustain. Chem. Eng.* **2016**, *4* (3), 1439–1445. https://doi.org/10.1021/acssuschemeng.5b01425.

(79) Stephenson, Richard M.; Malanowski, Stanislaw. *Handbook of the Thermodynamics of Organic Compounds*, 1st ed.; Springer Dordrecht, 1987.